

NUMERICAL SIMULATION OF A THREE-LAYERED RADIANT POROUS HEAT EXCHANGER INCLUDING LATTICE BOLTZMANN SIMULATION OF FLUID FLOW

E. Jahanshahi Javaran, S.A. Gandjalikhan Nassab and S. Jafari*

*Department of Mechanical Engineering, Shahid bahonar University
P.O.Box 75914, Kerman, Iran
Hamed.8556@gmail.com, Ganj110@uk.ac.ir, s.jafari@uk.ac.ir*

*Corresponding Author

(Received: January 26, 2011 – Accepted in Revised Form: September 23, 2011)

doi: 10.5829/idosi.ije.2011.24.03a.09

Abstract This paper deals with the hydrodynamic and thermal analysis of a new type of porous heat exchanger (PHE). This system operates based on energy conversion between gas enthalpy and thermal radiation. The proposed PHE has one high temperature (HT) and two heat recovery (HR₁ and HR₂) sections. In HT section, the enthalpy of flowing high temperature gas that is converted to thermal radiation emitted towards the two heat recovery sections where the reverse energy conversion from thermal radiation to gas enthalpy takes place. In each section, a 2-D rectangular porous segment which is assumed to be absorbing, emitting and scattering is present. For theoretical analysis of the PHE, the gas and solid are considered in non-local thermal equilibrium and separate energy equations are used for the two phases. Besides, in the gas flow simulation, the lattice Boltzmann method (LBM) is applied to obtain the velocity distribution through the porous segments. For the purpose of thermal analysis of the proposed PHE, volume-averaged velocities through the porous matrix obtained by LBM are used in the gas energy equation, and then the coupled energy equations for gas and porous medium of each section are numerically solved using finite difference method. The radiative transfer equation is solved by discrete ordinates method to calculate the distribution of radiative heat flux in the porous medium. The numerical results consist of the gas and porous media temperature distributions. The variation of radiative heat flux are also presented. Furthermore, the effects of scattering albedo, optical thickness and inlet gas temperature on the efficiency of the proposed PHE are investigated. It is revealed that this type of heat exchanger has high efficiency in comparison to conventional one. Also, the present numerical results for a porous radiant burner are compared with theoretical finding by the other investigator and good agreement is found.

Keywords Porous Heat Exchanger, Lattice Boltzmann Method, Discrete Ordinates Method

چکیده در این مقاله یک مدل از مبدل حرارتی متخلخل مورد بررسی قرار گرفته که اصول کارکرد آن بر اساس تبدیل انتالپی گاز به انرژی تابشی و بالعکس، میباشد. این مبدل شامل یک بخش مرکزی با درجه حرارت بالا و دو بخش بازیاب بوده که در هر کدام از این بخشها یک لایه متخلخل موجود میباشد. گاز داغ ورودی به مبدل حرارتی از درون لایه متخلخل در بخش مرکزی گذشته و انتالپی گاز به انرژی تابشی تبدیل میگردد. این انرژی تابشی به سمت بخشهای بازیاب گسیل داشته شده جایی که انرژی تابشی جذب شده بصورت افزایش انتالپی گاز ظاهر میشود. جهت آنالیز حرارتی این مبدل در هر بخش، محیط متخلخل با هندسه دو بعدی مستطیل شکل در نظر گرفته شده است. از آنجا که تعادل حرارتی بین فاز گاز و جامد وجود ندارد. معادلات انرژی به طور جداگانه برای هر فاز نوشته شده و بصورت همزمان حل شده اند. بعلاوه برای شبیه سازی جریان گاز و محاسبه متوسط حجمی سرعت سیال در داخل ماتریس متخلخل از LBM استفاده شده است. معادلات انرژی برای گاز و محیط متخلخل بصورت عددی با کمک روش اختلاف محدود حل عددی شده اند و جهت محاسبه توزیع شار تابشی در لایه متخلخل که از حل معادله انتقال حرارت تابشی به دست می آید از روش راستاهاى مجزا بهره برده شده است. نتایج عددی به صورت نمودارهایی از توزیع دمای گاز و محیط متخلخل و همچنین توزیع شار تابشی در فاز جامد ارائه شده اند و اثر پارامترهای متعددی بر رفتار حرارتی سیستم بررسی شده است. در عین سادگی ساختمان داخلی این مبدل، نتایج محاسبات عملکرد بالایی را برای این سیستم پیش بینی مینماید. جهت بررسی صحت محاسبات انجام شده، در مورد یک سیستم مشعل متخلخل تابشی، مقایسه ای با نتایج تئوریک دیگر محققین صورت پذیرفته که انطباق موجود رضایت بخش بوده است.

1. INTRODUCTION

Transport phenomena in porous media arise in many fields of science and engineering. In recent years, porous media have frequently been used in high temperature systems, such as heat recovery systems, porous radiant burners and porous heat exchangers. The technique of energy conversion between gas enthalpy and thermal radiation by means of porous medium has been studied by many researchers [1,2]. When a high temperature gas flows through a porous metal plate with high porosity, the enthalpy of working gas is effectively transformed to the porous medium via an extremely high heat transfer coefficient and large surface area between the flowing gas and the porous plate, and then a large amount of radiant energy is emitted in upstream direction by the porous plate with strong emissive power. This procedure has been used in high temperature heat exchangers to enhance the performance of these equipments [3].

Average and local surface heat transfer coefficients in a cylinder packed with spheres has been investigated experimentally by Khoshravan [4]. The experimental technique consisted of introducing a step-wise change in the temperature of air flowing through the bed and recording the resulting air and ball temperature transients within the bed over a range of Reynolds numbers. Finally, an overall correlation of heat transfer with Reynolds number was derived.

Yoshida, et al [5] investigated the transient characteristics of heat transfer in porous media. In that work, because of high porosity of the porous media, the conduction heat transfer in the radiative converter was neglected. In the non-radiating gas flow analysis, it was assumed that conduction and convection occurs simultaneously and integral method was used to obtain the net radiative heat flux in the porous matrix. Transient heat transfer characteristics of an energy recovery system using porous media has been investigated by Gandjalikhan Nassab [6] in which the two-flux radiation model was used to calculate the radiative fluxes.

Based on the energy conversion technique between gas enthalpy and thermal radiation, a new type of multi layered gas-to-gas porous heat

exchanger has been proposed by Tomimura et al. [7]. A series of experiments have been conducted for 2-5 layers and it was clarified that the optical thickness of about 8 is enough to obtain sufficient heat recovery.

A multi-layered type of porous air heater was proposed by the author [8]. The proposed system has five distinct porous layers which are separated from each other by four quartz glass walls. The heat of combustion is converted into thermal radiation in a porous radiant burner and the energy conversion process from thermal radiation into gas enthalpy occurred in low temperature sections. In order to improve the thermal performance of the system, a high temperature section was also considered to recover the enthalpy of exhaust gas from PRB which otherwise would be wasted. Two-flux model was used to describe the radiative flux from the solid matrix. Numerical results showed a very high efficiency for this type of porous air heater.

A five-layered porous heat exchanger consisting of two high temperature, two heat recovery and one low temperature sections have been analyzed by Gandjalikhan Nassab, et al [9]. In that work, the gaseous radiation was also considered and it was shown that in the case of high optical thicknesses for porous layers, this type of porous heat exchanger has high efficiency. In a recent study by the second author, theoretical analysis of a porous radiant burner under the influence of a 2-D radiation field using discrete ordinates method was carried out [10]. In that work, combustion in the porous medium was modeled by considering a non-uniform heat generation zone. It was found that the layer with large aspect ratio and small scattering coefficient, operates efficiently to convert the energy from gas enthalpy to thermal radiation. Also, the results indicate that the temperatures of gas and porous media at the outlet section increase as the flame location moves downstream.

In all of the above works, for obtaining the gas and temperature distributions along the porous layer, the gas and energy equations was solved numerically, such that the convective term in gas energy equation was considered by assuming a simple plug flow through porous matrix. Besides, it is clear that to achieve an accurate thermal analysis, fluid flow simulation in porous medium should be considered. Complex geometry of a porous medium

makes it difficult to simulate flow using conventional methods such as the finite difference, finite volume, and finite element methods. The lattice Boltzmann method, which is a new method for simulating fluid flow and modeling physics in fluids, has successfully been applied to simulate flow in porous media [11]. Two approaches have been adopted in simulations of porous flow using LBM; the pore-scale approach and the representative elementary volume (REV)-scale approach [12]. In the first approach, the fluid through the pores of the medium is directly modeled by the standard LBM and no-slip bounce-back rule is applied to account for interaction between fluid and solid. In the REV approach, an extra term is added to the standard LBM to show the presence of the porous medium. In 1989, three-dimensional flow in complex geometries with the lattice Boltzmann method was simulated by Succi et al [13]. In that work, Darcy's law was recovered and a preliminary estimation of the permeability presented. Numerical simulations of the lattice Boltzmann equation in three-dimensional porous geometries constructed by the random positioning penetrable spheres of equal radii were investigated by Cancelliere et al [14] and methods for calculating the permeability were presented. A lattice Boltzmann description of fluid flow in heterogeneous porous media was presented by Spaid and Phelan [15]. In that study, the Brinkman equation was also recovered through a modification of the particle equilibrium distribution function. Guo and Zhao [12], proposed a lattice Boltzmann model for isothermal incompressible flow in porous media. The key point was to include the porosity into the equilibrium distribution function, and add a force term in the evolution equation to account for the linear and nonlinear drag forces of the medium (Darcy and Forcheimer terms). Through the Chapman-Enskog procedure, the generalized Navier-Stokes equations for incompressible flow in porous media were derived from the lattice Boltzmann model.

The capability and accuracy of the lattice Boltzmann equation (LBE) for modeling flow through porous media was investigated by Pan et al [16]. In that work, several fluid-solid boundary conditions were investigated. They also conducted a comparative study of LBE models with the multiple-relaxation time (MRT) and Bhatnagar-Gross-Krook (BGK) single relaxation time (SRT) collision operators and found that MRT-LBE model

is superior to the BGK- LBE model. Yan et al [17] numerically studied the porous flow through low head loss biofilter medium using the lattice Boltzmann method. The constant pressure drop was set by giving the same density difference between the inlet and outlet of the biofilter and the effects of Darcy number and porosity on removal efficiency of low head loss biofilter were investigated. Three-dimensional fluid flow simulations in fibrous media were conducted using the SRT LBM by Nabovati et al [18]. The fibrous media were constructed by random placement of cylindrical fibers with random orientations within the computational domain. The radius, curvature and length of the fibers were varied systematically. It was found that fiber curvature has a negligible impact on the permeability of the medium.

According to the literature and to the best of authors' knowledge, the thermal characteristics of porous heat exchangers have not been obtained by solving the flow equation using LBM. The purpose of the present work is to develop a mathematical model to investigate the thermal and hydrodynamic behaviors of a new type of PHE using porous media. The heat exchanger consists of three distinct rectangular porous segments called HT, HR₁ and HR₂ sections. These segments are separated from each other by two quartz glass windows. In the HT section, the enthalpy of flowing high temperature gas is converted to thermal radiation and in heat recovery sections, the reverse energy conversion from thermal radiation into gas enthalpy take place, such that entering air flow to the heat exchanger is heated in two steps in HR₁ and HR₂ respectively. The schematic outline of the system is shown in Figure 1. The lattice Boltzmann method is employed to obtain the gas velocity field through the porous segments. Furthermore, in thermal analysis of the PHE, because of the non-local thermal equilibrium between gas and solid phases, separate energy equations for both phases are solved by numerical techniques. To obtain the radiative term in the porous energy equation, the radiative transfer equation is solved numerically by discrete ordinates method (DOM). For validation of computational results, comparison is made between the present numerical results with those obtained theoretically by other investigators for a porous radiant burner and good agreement is found.

2. THEORETICAL ANALYSIS

The basis of the proposed PHE, which consists of one high temperature section and two heat recovery sections, is the energy conversion process between flowing gas enthalpy and thermal radiation, such that similar processes take place in all three sections. To save space, only the detailed theoretical analysis of the HT section is detailed here; similar methods are applied to heat recovery sections. In Figure 2, a schematic diagram of the flowing gas passing through a porous segment is shown. A high porosity non-homogeneous rectangular porous segment with the dimensions L_x and L_y is located in the region $0 < x < L_x$ through the channel. To ensure the two dimensionality of the problem, dimensions of the channel and porous medium in normal direction to the gas flow (not shown here) are remarkably large. The HT gas flow with uniform velocity and temperature distribution enter the channel at $x = -x_i$. The incoming radiation fluxes B_1 and B_2 from upstream and downstream directions are considered as incident radiation to the porous segment. The porous medium is considered as a radiating medium that emits, absorbs and scatters thermal radiation while gaseous radiation is neglected in comparison to solid radiation. Therefore, radiation is considered only between the particles that comprise the porous segment. All thermo physical properties of the solid and gas phases are assumed constant. To obtain thermal behavior of the proposed PHE, the gas velocity distribution through porous segments is needed. This part of simulation is carried out by employing the lattice Boltzmann method.

2.1. Hydrodynamic Computations by Means of Lattice Boltzmann Method

2.1.1. Theory of lattice boltzmann method In the present work, the lattice Boltzmann equation with the multiple-relaxation-time (MRT) is used [19,20],

$$\mathbf{f}(x_i + e\delta t, t + \delta t) = \mathbf{f}(x_i, t) - M^{-1} \cdot \hat{S} \cdot [\mathbf{m} - \mathbf{m}^{eq}(\rho, u)](x_i, t) \quad (1)$$

in which ρ and u are the macroscopic density and velocity respectively, the bold face symbols such as \mathbf{f} stand for 9-component vectors; 9 is the

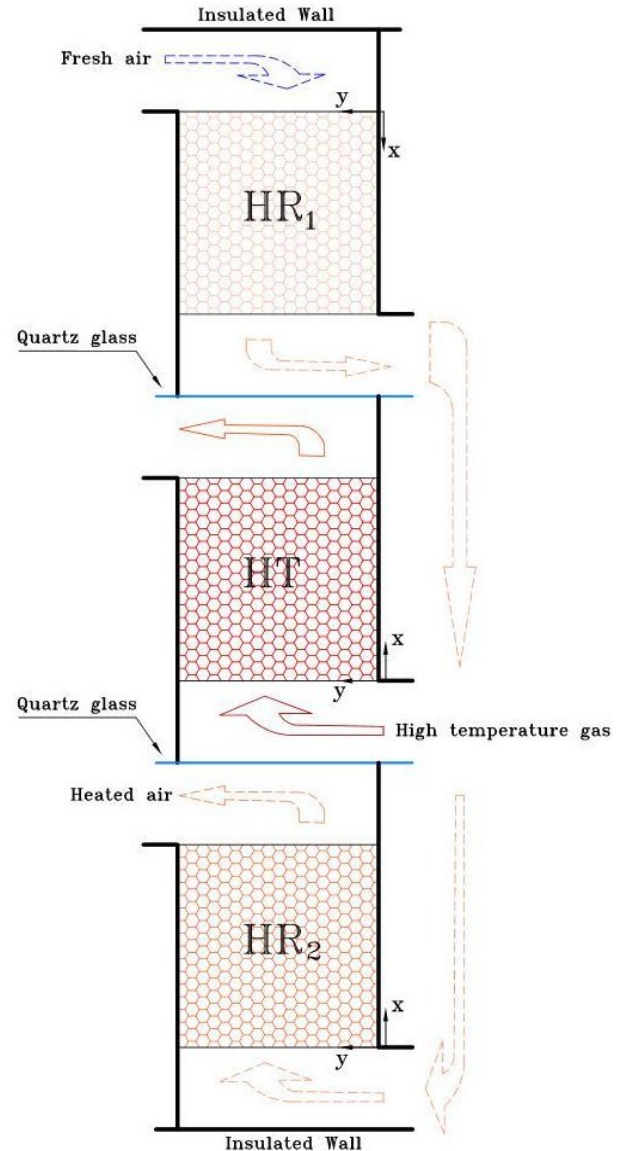


Figure 1. Schematic diagram of a three-layered porous heat exchanger.

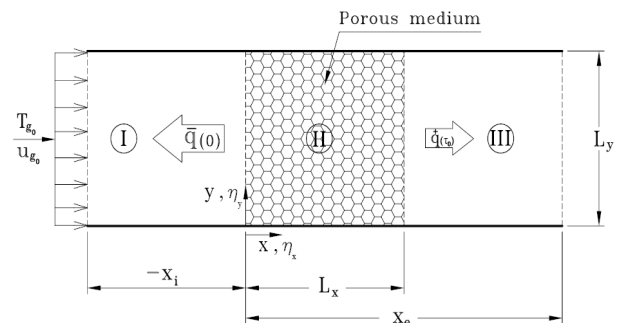


Figure 2. Schematic sketch of a single layer of the PHE.

number of discrete velocities, as follows:

$$\mathbf{f} = (f_0, f_1, \dots, f_8)^T \quad (2)$$

$$\mathbf{f}(x_i + e\delta t) = (f_0(x_i), f_1(x_i + e\delta t), \dots, f_8(x_i + e\delta t))^T \quad (3)$$

$$\mathbf{m} = (m_0, m_1, \dots, m_8) \quad (4)$$

$$\mathbf{m}^{eq} = (m_0^{eq}, m_1^{eq}, \dots, m_8^{eq}) \quad (5)$$

where T denotes the transpose operator. In Equation 1, \mathbf{f} is the 9-component vector of the discrete distribution functions, \mathbf{m} and \mathbf{m}^{eq} are 9-component vectors of moments and their equilibria, M is the transformation matrix and \hat{S} is the diagonal matrix of relaxation rates.

The nine-velocity square lattice Boltzmann (D_2Q_9) model has widely and successfully been used for simulating two-dimensional flows (Figure 3). In the (D_2Q_9) model, e_α denotes the discrete velocity set, namely,

$$e_0 = (0, 0) \quad (6a)$$

$$e_\alpha = (\pm 1, 0)c \text{ and } (0, \pm 1)c \quad \text{for } \alpha = 1, 2, 3, 4 \quad (6b)$$

$$e_\alpha = (\pm 1, \pm 1) \quad \text{for } \alpha = 5, 6, 7, 8 \quad (6c)$$

where $c = \delta x / \delta t$, δx and δt are the lattice spacing and the time increment which are assumed to be unity.

The moments are arranged in the following order:

$$\mathbf{m} = (\rho, e, \varepsilon, j_x, q_x, j_y, q_y, p_{xx}, p_{xy})^T \quad (7)$$

where $m_0 = \rho$ is the density, $m_1 = e$ is related to the total energy, $m_2 = \varepsilon$ is related to energy square, $(m_3, m_5) = (j_x, j_y) = \rho(u_x, u_y)$ is the flow momentum, $(m_4, m_6) = (q_x, q_y)$ is related to the heat flux, and $m_7 = p_{xx}$ and $m_8 = p_{xy}$ are related to the diagonal and off-diagonal components of the stress tensor, respectively.

The macroscopic density and momentum on each lattice node are calculated using the following equations:

$$\rho = \sum_{\alpha=0}^8 f_\alpha \quad (8)$$

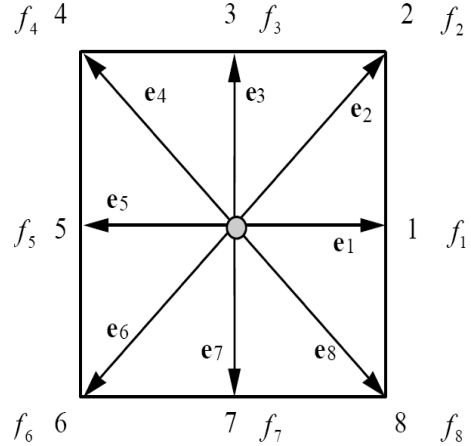


Figure 3. A 2-D 9-velocity lattice (D_2Q_9) model.

$$\mathbf{j} = \rho \mathbf{u} = \sum_{\alpha=1}^8 e_\alpha f_\alpha \quad (9)$$

In addition, in Equation 1, the equilibrium moments are:

$$e^{eq} = -2\rho + 3(j_x^2 + j_y^2), \quad \varepsilon^{eq} = \rho - 3(j_x^2 + j_y^2) \quad (10)$$

$$q_x^{eq} = -j_x, \quad q_y^{eq} = -j_y \quad (11)$$

$$p_{xx}^{eq} = j_x^2 - j_y^2, \quad p_{xy}^{eq} = j_x j_y \quad (12)$$

The transform matrix is given as follows [19]:

$$M = \begin{bmatrix} 1 & 1 & 1 & 1 & 1 & 1 & 1 & 1 & 1 \\ -4 & -1 & -1 & -1 & -1 & 2 & 2 & 2 & 2 \\ 4 & -2 & -2 & -2 & -2 & 1 & 1 & 1 & 1 \\ 0 & 1 & 0 & -1 & 0 & 1 & -1 & -1 & 1 \\ 0 & -2 & 0 & 2 & 0 & 1 & -1 & -1 & 1 \\ 0 & 0 & 1 & 0 & -1 & 1 & 1 & -1 & -1 \\ 0 & 0 & -2 & 0 & 2 & 1 & 1 & -1 & -1 \\ 0 & 1 & -1 & 1 & -1 & 0 & 0 & 0 & 0 \\ 0 & 0 & 0 & 0 & 0 & 1 & -1 & 1 & -1 \end{bmatrix} \quad (13)$$

This matrix maps the distribution functions to their moments in the following form:

$$\mathbf{m} = M \mathbf{f}, \quad \mathbf{f} = M^{-1} \mathbf{m} \quad (14)$$

The diagonal matrix \hat{S} of relaxation rates $\{s_i\}$ is given by:

$$\hat{S} = \text{diag}(0, s_1, s_2, 0, s_4, 0, s_6, s_7, s_8) \quad (15)$$

where the relaxation rates $s_7 = s_8 = 1/\tau$ determines the dimensionless viscosity of the model:

$$\nu = (\tau - \frac{1}{2})c_s^2 \delta t \quad (16)$$

The speed of sound in D₂Q₉ model is $c_s = c/\sqrt{3}$. Pressure and density are related to each other by the equation of state for an ideal gas, $P = \rho c_s^2$. Other relaxation rates s_1, s_2 and $s_4 = s_6 = s_q$ are usually indicated by linear stability of the model [19]. In addition, the no-slip boundary conditions will also determine the choice of $s_4 = s_6$ [16].

With the above equilibrium moments, if all relaxation rates are set to be a single value $1/\tau$, i.e., $\hat{S} = \tau^{-1}I$, where I is 9×9 identity matrix, then the model is equivalent to an LBGK model with the following equilibrium distribution function:

$$f_\alpha^{(eq)} = \rho w_\alpha [1 + \frac{3}{c^2} e_\alpha \cdot u + \frac{9}{2c^4} (e_\alpha \cdot u)^2 - \frac{3}{2c^2} u \cdot u] \quad (17)$$

For D₂Q₉ model, the coefficients $w_0 = 4/9$, $w_i = 1/9$ for $i = 1-4$, and $w_i = 1/36$ for $i = 5-8$.

2.1.2. Methodology for simulating fluid flow in 2-D porous media In the present study, the fluid flow in two-dimensional random porous media is simulated at pore level scale using LBM. The problem under consideration is depicted in Figure 2. The channel is divided into three sections I, II and III. Two-dimensional square obstacles with random distribution are placed in section II between two parallel plates to produce desired porosity. The random generator must distribute solid obstacles in the domain monotonously with free overlapping and its porous generation differs, when it runs at different times. A void fraction function $P(x)$ is used to differentiate solid nodes from fluid nodes:

$$P(x) = \begin{cases} 0 & \text{fluid} \\ 1 & \text{solid} \end{cases} \quad (18)$$

To solve Equation 1, suitable boundary conditions should be considered. The boundary conditions are specific velocity and pressure at the inlet and outlet sections, respectively; no-slip boundary condition at solid-fluid interactions (upper and lower walls

and solid-fluid boundaries in the interior domain). Since, in the lattice Boltzmann computations, the unknowns are distribution functions, therefore, these boundary conditions should be represented in the form of distribution functions. At the inlet and outlet sections of the domain, the method proposed by Lim et al. [21] is used to demonstrate the given boundary conditions in terms of the distribution functions as follows:

Inlet boundary conditions:

$$\begin{aligned} f_1(x=0, y, t) &= f_1^{eq}(\rho, u = u_{inlet}, v = 0, x = 0, y, t) \\ f_2(x=0, y, t) &= f_2^{eq}(\rho, u = u_{inlet}, v = 0, x = 0, y, t) \\ f_8(x=0, y, t) &= f_8^{eq}(\rho, u = u_{inlet}, v = 0, x = 0, y, t) \end{aligned} \quad (19)$$

Outlet boundary conditions:

$$\begin{aligned} f_5(LX, y, t) &= f_5^{eq}(\rho_{out}, u, v, x = LX, y, t) \\ f_4(LX, y, t) &= f_4^{eq}(\rho_{out}, u, v, x = LX, y, t) \\ f_6(LX, y, t) &= f_6^{eq}(\rho_{out}, u, v, x = LX, y, t) \end{aligned} \quad (20)$$

Owing to the specific velocity boundary condition at the inlet, the values of u, v are known at this nodes and the density values are extrapolated from the flow domain whereas at the outlet, density values are given due to the equation of state, and the u - and v -values are obtained using a second order extrapolation from the interior domain. The bounce-back boundary condition is used at lower and upper walls and the solid-fluid interaction in the interior domain:

$$f_{\bar{\alpha}}(x_f, t + \delta t) = f_\alpha(x_f, t) \quad (21)$$

where x_f is the fluid node next to the boundary location x_b and $e_\alpha = -e_{\bar{\alpha}}$. It was shown that the no-slip boundary location is precisely on half lattice spacing beyond the last flow node, if the following relation is satisfied [16]:

$$s_q = 8 \frac{(2 - s_v)}{(8 - s_v)} \quad (22)$$

in which $s_v = s_7 = s_8 = 1/\tau$ determines the shear viscosity and $s_4 = s_6 = s_q$ is the relaxation rate for q_x and q_y . It is obvious that the single-relaxation-time collision model can not satisfy this condition.

These boundary conditions with the evolution equation (Equation 1) are used to simulate fluid flow in the porous medium.

2.1.3. Results and confirmation of the fluid flow computations

This section shows the main results of the fluid flow simulation. Dimensions of the channel were chosen $0.09 \times 0.03 \text{ m}^2$ (length \times height) and obstacle size (d_p) was 0.4 mm (4-lattice unit). Calculations were performed using 900×300 lattice nodes for $Re_{L_x} = 450$.

Porosity was assumed to be 0.9 in this study.

Velocity profiles along x-axis at different cross sections through the channel are shown in Figure 4. Moreover, to demonstrate the effect of obstacles on the fluid flow, the zoomed observation of the velocity field and streamlines in the porous medium are shown in Figures 5a, 5b. The effect of solid particles on flow distribution is clearly seen in these figures.

To verify the numerical results, the non-dimensional pressure drop ($-dP/dX$) along the porous medium was compared with the results of other investigators. In order to calculate ($-dP/dX$), the non-dimensional pressure difference between the inlet and outlet of the porous matrix is divided by its non-dimensional length. The inlet and outlet fluid pressures are determined using the following equation

$$P = \frac{\sum_{j=1}^{j \max} P_j}{j \max} \quad (23)$$

In addition, pressure drop computations are carried out using Darcy law with Forchheimer term which is as follows [22-24]:

$$-\nabla \tilde{P} = \frac{\mu}{\kappa} u_{g_0} + A \rho u_{g_0}^2 \quad (24)$$

where parameter A in Equation 24 is an empirical function given by:

$$A = \frac{1.75(1-\phi)}{\phi^3 d_p} \quad (25)$$

To determine the permeability κ , the two following forms are used:

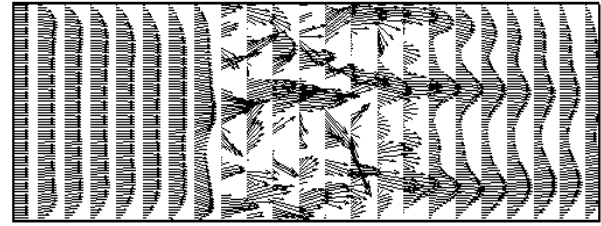
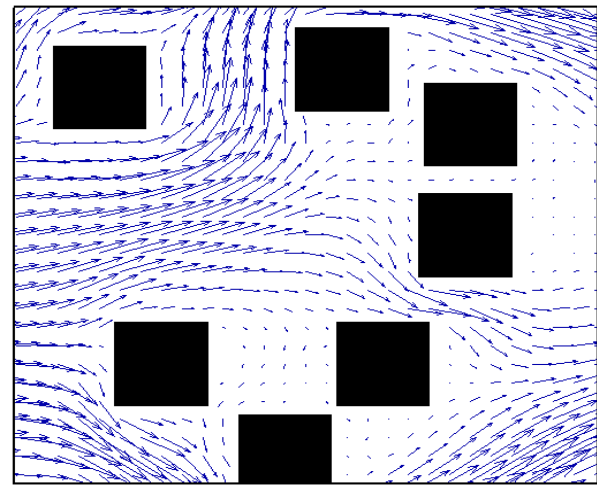
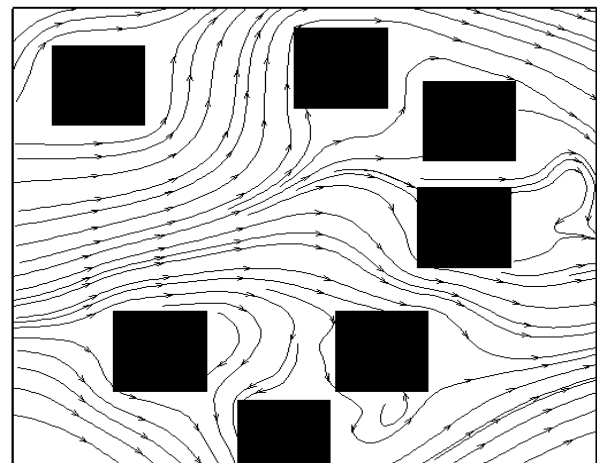


Figure 4. Velocity vectors in a duct including porous segment, $Re_{L_x} = 450$.



(a)



(b)

Figure 5. (a) Vector field inside the porous medium, (b) streamlines inside the porous medium, $\phi = 0.9$.

$$k = \frac{\phi^3 d_p^2}{150(1-\phi)^2} \quad (26)$$

$$k = \frac{\phi^3 d_p^2}{175(1-\phi)^2} \quad (27)$$

The non-dimensional pressure gradient ($-dP/dX$) through the porous medium versus Re_p for $\phi = 0.9$ is shown in Figure 6. It is seen that there is quite a good agreement between the pressure drop calculations of the present analysis and those calculated based on Equation 24.

In addition, to investigate the grid dependency of the results, three different sizes of domain and obstacles were used: 4×4 obstacles in a 360×120 domain, 5×5 obstacles in a 450×150 domain and 6×6 obstacles in a 540×180 domain. The non-dimensional pressure gradients for these three grids are summarized in Table 1. The difference between second and third grid is below 1%. Therefore, we use the second one to validate our results. In addition, we created 12 media with different random obstacle placement for 450×150 domain and the Reynolds number of 450. The mean non-dimensional pressure gradient and standard deviation for these media are shown in Table 2. The comparison between the non-dimensional pressure gradient for the random and uniform porous medium in Table 1 and the mean non-dimensional pressure gradient for these media shows relatively good agreement.

2.2. Thermal Computations

2.2.1. Governing equations Since the gas and solid phases are not in local thermal equilibrium, separate energy equations are needed to describe energy transfer in these two phases. To this end, the gas and porous media energy equations are obtained with volumetric averaging, but for only a small control volume ΔV that contains a number of solid particles. Besides, the energy balance for the gas flow and the solid phase are written by considering the convective energy transfer between two phases with a known convection coefficient. This coefficient which is a function of gas velocity and particle size is calculated by empirical equations given in Ref. [25].

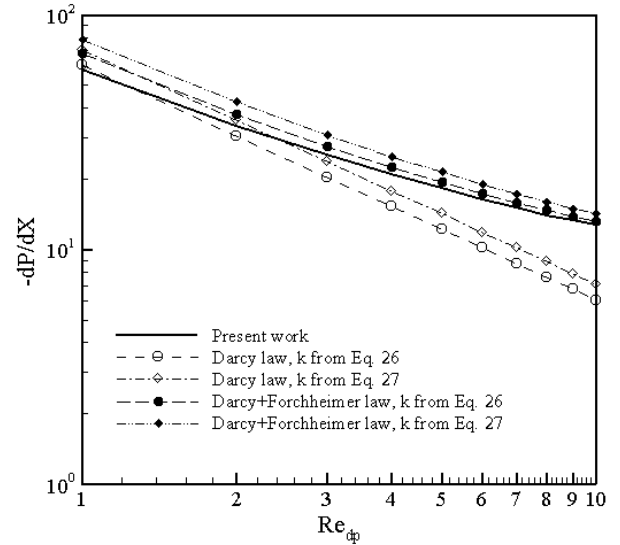


Figure 6. Variation of non-dimensional pressure gradient with Re_p along porous medium ($\phi = 0.9$).

TABLE 1. The Non-Dimensional Pressure Gradient for Different Grids.

Grid	Obstacle	Non-Dimensional Pressure Gradient
360×120	4×4	17.9890
450×150	5×5	16.5135
540×180	6×6	16.4015

TABLE 2. Mean Non-Dimensional Pressure Gradient and Standard Deviation For Different Media.

Porosity	Mean Non-Dimensional Pressure Gradient	Standard Deviation (%)
0.9	17.5418	6.47

The energy equations for gas and solid phases along with the radiative transfer equation can be written in non-dimensional forms as follows:

$$\frac{\phi}{Pe} \left(\frac{\partial^2 \theta_g}{\partial \eta_x^2} + \frac{\partial^2 \theta_g}{\partial \eta_y^2} \right) - \left(U \frac{\partial \theta_g}{\partial \eta_x} + V \frac{\partial \theta_g}{\partial \eta_y} \right) - P_1 (\theta_g - \theta_p) = 0 \quad (28)$$

$$(1-\phi)P_2\left(\frac{\partial^2\theta_p}{\partial\eta_x^2}+\frac{\partial^2\theta_p}{\partial\eta_y^2}\right)-\nabla\cdot Q_{rad}+P_3(\theta_g-\theta_p)=0 \quad (29)$$

$$\hat{s}\cdot\nabla I^*(\vec{r},\hat{s})=-\tau_0 I^*(\vec{r},\hat{s})+\tau_1 I^*_b(\vec{r})+\frac{\tau_2}{4\pi}\int_{\omega=4\pi} I^*(\vec{r},\hat{s}')\phi(\vec{r},\hat{s},\hat{s}')d\Omega' \quad (30)$$

It should be noted that all variables and non-dimensional parameters used in these equations and their boundary conditions are given in the Nomenclature.

The non-dimensional divergence of radiative heat flux, $\nabla\cdot Q_{rad}$, can be obtained from the radiative transfer equation (Equation 30) and is written in the following form:

$$\nabla\cdot Q_{rad}=\left(\frac{\partial Q_{rad_x}}{\partial\eta_x}+\frac{\partial Q_{rad_y}}{\partial\eta_y}\right) \quad (31)$$

Solving Equation 30 leads to find unknown intensities, which are used for obtaining the radiative heat flux inside the medium as follows:

$$Q_{rad}(\vec{r})=\int_{4\pi} I^*(\vec{r},\hat{s})\hat{s}d\Omega \quad (32)$$

2.2.2. Boundary conditions In order to solve the governing equations, the following boundary conditions are employed.

Gas phase boundary conditions:

The following boundary conditions are applied at four boundary surfaces

$$\eta_x=0, \quad \eta_x=1, \eta_y=0 \quad \text{and} \quad \eta_y=\eta_{Ly}$$

$$\theta_g=\theta_{g0} \quad \text{at} \quad \eta_x=0 \quad (33)$$

$$\frac{\partial\theta_g}{\partial\eta_x}=Nu(\theta_p-\theta_g) \quad \text{at} \quad \eta_x=1 \quad (34)$$

$$\frac{\partial\theta_g}{\partial\eta_y}=P_5(\theta_g-\theta_\infty) \quad \text{at} \quad \eta_y=0 \quad (35)$$

$$\frac{\partial\theta_g}{\partial\eta_y}=-P_5(\theta_g-\theta_\infty) \quad \text{at} \quad \eta_y=\eta_{Ly} \quad (36)$$

Solid phase boundary conditions:

For the solid energy equation, two energy

balances at the inlet and outlet sections give the following two boundary conditions:

$$Bi(\theta_{g0}-\theta_p)+\frac{\varepsilon_p}{P_2}(\theta_i^4-\theta_p^4)=-\frac{\partial\theta_p}{\partial\eta_x} \quad \text{at} \quad \eta_x=0 \quad (37)$$

$$Bi(\theta_p-\theta_g)+\frac{\varepsilon_p}{P_2}(\theta_p^4-\theta_o^4)=-\frac{\partial\theta_p}{\partial\eta_x} \quad \text{at} \quad \eta_x=1 \quad (38)$$

On the upper and lower walls, the following boundary conditions are considered:

$$\frac{\partial\theta_p}{\partial\eta_y}=P_4(\theta_p-\theta_\infty) \quad \text{at} \quad \eta_y=0 \quad (39)$$

$$\frac{\partial\theta_p}{\partial\eta_y}=-P_4(\theta_p-\theta_\infty) \quad \text{at} \quad \eta_y=\eta_{Ly} \quad (40)$$

Radiative transfer boundary conditions:

To solve the radiative transfer equation, appropriate boundary conditions are needed which are as follows:

$$I^{*m}(0,\eta_y)=\frac{B'_1}{\pi} \quad \text{at} \quad \eta_x=0 \quad (41)$$

$$I^{*m}(1,\eta_y)=\frac{B'_2}{\pi} \quad \text{at} \quad \eta_x=1 \quad (42)$$

$$I^{*m}(\eta_x,0)=\varepsilon_B\frac{\sigma\theta_B^4}{\pi}+\frac{\rho_B}{\pi}\int_{\hat{n}\cdot\hat{s}'<0}|\hat{n}\cdot\hat{s}'|I^*(\eta_x,0,\hat{s}')d\Omega' \quad \text{at} \quad \eta_y=0 \quad (43)$$

$$I^{*m}(\eta_x,\eta_{Ly})=\varepsilon_T\frac{\sigma\theta_T^4}{\pi}+\frac{\rho_T}{\pi}\int_{\hat{n}\cdot\hat{s}'<0}|\hat{n}\cdot\hat{s}'|I^*(\eta_x,\eta_{Ly},\hat{s}')d\Omega' \quad \text{at} \quad \eta_y=\eta_{Ly} \quad (44)$$

3. SOLUTION METHOD

3.1. Discrete Ordinates Method (S_N Approximation) The discrete ordinates method, which is a numerical and straightforward technique to solve the radiative transfer equation (RTE), transforms the equation of transfer into a set of partial differential equations [26]. This method is based on a discrete representation of the radiation

intensity in specified directions. The notation S_N approximation indicates that N different direction cosines which are used for each principal direction, such that $n = N(N+2)$ different directions should be considered for all radiant intensities. According to this method, the general equation of transfer (Equation 30) is solved for a set of n different directions \hat{s}_i , $i=1, 2, \dots, n$, along the total solid angle range of 4π , such that the integrals over direction are replaced by quadratures as follows:

$$\int_{4\pi} f(\hat{s}) d\Omega \approx \sum_{i=1}^n w_i f(\hat{s}_i) \quad (45)$$

where the w_i s are the quadrature weights associated with the directions \hat{s}_i .

Therefore, the RTE is approximated by a set of n differential equations as follows:

$$\hat{s}_i \cdot \nabla I^*(\vec{r}, \hat{s}_i) = -\tau_0 I^*(\vec{r}, \hat{s}_i) + \tau_1 I_b^*(\vec{r}) + \frac{\tau_2}{4\pi} \sum_{j=1}^n w_j I^*(\vec{r}, \hat{s}_j) \varphi(\vec{r}, \hat{s}_i, \hat{s}_j) \quad i = 1, 2, \dots, n \quad (46)$$

Once the intensities have been determined in the desired directions, integrated quantities can be readily calculated. Then, the radiative flux method inside the medium may be found from:

$$Q_{rad}(r) = \int_{4\pi} I^*(r, \hat{s}_i) \hat{s}_i d\Omega \approx \sum_{i=1}^n w_i I_i^*(r) \hat{s}_i \quad (47)$$

For the two-dimensional Cartesian coordinates system, Equation 46 becomes

$$\xi^m \frac{\partial I^{*m}}{\partial \eta_x} + \eta^m \frac{\partial I^{*m}}{\partial \eta_y} = -\tau_0 I^{*m} + \tau_1 I_b^* + \frac{\tau_2}{4\pi} \sum_{m'} w^{m'} \varphi^{m'm} I^{*m'} \quad (48)$$

in which m and m' denote outgoing and incoming directions, respectively.

The following equation can be obtained for computing radiant intensity by differentiation of the above equation:

$$I_{i,j}^{*m} = \frac{IX^m + IY^m + \tau_1 I_{b,i,j}^* + S^{*m}}{\tau_0 + X^m \text{Sign}(X^m) + Y^m \text{Sign}(Y^m)} \quad (49)$$

where

$$IX^m = X^m u_0(X^m) I_{i-1,j}^{*m} - X^m u_0(-X^m) I_{i+1,j}^{*m}$$

$$IY^m = Y^m u_0(Y^m) I_{i,j-1}^{*m} - Y^m u_0(-Y^m) I_{i,j+1}^{*m}$$

$$X^m = \frac{\xi^m}{\Delta \eta_x}$$

$$Y^m = \frac{\eta^m}{\Delta \eta_y}$$

$$S^{*m} = \frac{\tau_2}{4\pi} \sum_m w^{m'} \varphi^{m'm} I_{i,j}^{*m'}$$

$$u_0(X) = \begin{cases} 1 & X > 0 \\ 0 & X < 0 \end{cases}$$

$$\text{Sign}(X) = \begin{cases} 1 & X > 0 \\ -1 & X < 0 \end{cases}$$

The numerical solution of Equation 48 can be started with the black body assumption for the boundaries with neglecting the source term S^* . In the following iterations, the general form of Equation 48 and its boundary conditions are applied. This procedure is repeated until the convergence criterion is met. Finally, from the radiative intensities obtained by Equation 49, the divergence of the radiative heat flux can be calculated from the following equation:

$$\nabla \cdot Q_{rad} = 4\pi \tau_1 \left(I_b^* - \frac{1}{4\pi} \sum_{m'} w^{m'} I^{*m'} \right) \quad (50)$$

The details of numerical solution of RTE by DOM were also described in the previous work by the author in which the thermal characteristic of porous radiant burner were investigated [8].

3.2. Solution Strategy Non-dimensional forms of governing equations are solved numerically to obtain the temperature and radiative heat flux distributions in three sections of the PHE. Equations 28 to 30 are coupled and should be solved simultaneously. To this end, the finite difference forms of gas and solid energy equations are obtained using central differencing for derivative terms where the error of discretization is of the order of Δx^2 and Δy^2 .

To solve the gas energy equation (Equation 28),

u - and v - velocity components at each nodal point through the porous medium are needed. These values are obtained using the lattice Boltzmann method. As mentioned in section 2.2.1, the energy equations are written by integral method, but for a differential control volume of $(dx \times dy)$ that comprises a number of solid particles based on the medium porosity. Considering this point, each control volume contains some pore and void nodes. Velocity values at these nodes are obtained using LBM and then by averaging the velocities of these nodes at each control volume (volume-averaged velocity), one can obtain the velocities that are used in gas energy equation. It should be noted that gas and solid energy equations along with radiative transfer equation are solved after the time-independent velocity are obtained by the lattice Boltzmann method. In addition, the radiative transfer equation is solved using discrete ordinates method, as mentioned before, to obtain the radiative term in the porous energy equation.

The sequence of calculations can be summarized as follows:

1. A first approximation of each dependent variable θ_g and θ_p is assumed.
2. The finite difference form of the radiative transfer equation is solved using S_6 approximation to obtain the values of I^* , Q_{rad} and ∇Q_{rad} at each nodal point.
3. The solid energy equation is solved to determine porous temperature θ_p using the values of ∇Q_{rad} obtained in step 2.
4. The values of θ_g are computed by numerical solution of the gas energy equation.
5. Steps 2-4 are repeated until convergence is achieved. This condition was assumed to be achieved when the fractional changes in the temperature and radiative intensity between the two consecutive iteration levels did not exceed 10^{-6} at each nodal point.

To fulfill the grid independent solution, a uniform grid of 80×60 nodal points in the computational domain is used.

3.3. Thermal Analysis of the Proposed PHE As shown in Figure 1, the PHE under investigation

consists of HT , HR_1 and HR_2 sections. In the HT section, the enthalpy of HT gas flow is effectively converted into thermal radiation and in two heat recovery sections the reverse conversion process from thermal radiation into gas enthalpy takes place.

In the preceding sections, the governing equations with the method of solution for analyzing a single porous layer were described in detail. In the structure of the proposed PHE, there are three layers that are similar to each other. Therefore, to analyze the proposed PHE, the same method that was used for a single porous layer in a duct can be applied to each of the three sections. Moreover, the temperature of the inlet gas into the HT , i.e. T_{g_0} , is considered as the reference temperature for all sections

In the numerical solution of each layer, the values of incoming radiations B_1 and B_2 , which are the boundary conditions for the radiative transfer equation, are needed to solve the RTE. In contrast, these incoming radiative fluxes are indeed the recaptured radiations $\bar{Q}_{rad}(\eta_x = 0)$ and $\bar{Q}_{rad}(\eta_x = 1)$ emitted from the adjacent layers, which are unknown before solving the set of governing equations. Therefore, the coupled set of governing equations for all sections must be solved simultaneously by an iterative method until the convergence criterion is met. The sequence of calculations can be stated as follows:

1. A first approximation of incoming radiations B_1 and B_2 to the HT section is assumed.
2. The coupled set of governing equations for the HT section are solved to calculate the values of \bar{Q}_{rad} , \bar{Q}_{rad} , θ_g and θ_p at each nodal point.
3. To analyze the HR_1 section, the value of B_2 as a boundary condition is needed. This parameter is equal to the emitted radiation from exit section of the HT layer, i.e. $\bar{Q}_{rad}(\eta_x = 1)$ (obtained in step 2), multiply to the configuration factor between two adjacent layers. Using this value, the coupled governing equations for the HR_1 section are solved. A similar procedure is applied to the

HR2 section, but the value of B'_2 is the emitted radiation from the entrance section of the HT layer, i.e. $\overline{Q_{rad}}(\eta_x = 0)$. It is assumed that the value of incident radiation B'_1 for both HR₁ and HR₂ sections is the reflected part of the incident radiation (irradiation) to the insulated walls according to the configuration factor between the entrance section of the HR₁ and HR₂ layers and insulated walls.

4. Using the computations in step 3, assumptions that was made for B'_1 and B'_2 will be modified.
5. Steps 2 to 4 are repeated until convergence criteria for all variables are fulfilled.

4. VALIDATION OF THE COMPUTATIONAL RESULTS

Since, we could not find any theoretical or experimental results for such a two-dimensional PHE in literature, the theoretical results of a 2-D porous radiant burner are used to validate the computer code written for the purpose of computations of the porous heat exchanger. It should be noted that the non-dimensional form of the governing equations for the porous radiant burner are the same as those used for the PHE apart from an additional term $\phi P_6 \delta(\eta_x)$ that includes the heat generation term (\dot{Q}) in the combustion zone of the radiant burner which must be added to the gas energy equation, where P_6 and $\delta(\eta_x)$ are as follows:

$$P_6 = \frac{\dot{Q} L_x}{T_{g0} \rho_g u_g c_g}$$

$$\delta(\eta_x) = \begin{cases} 1 & 0.5 < \eta_x < 0.5 + \Delta x_{flame} / L_x \\ 0 & elsewhere \end{cases}$$

Dimensions of the test case under consideration are $L_x = 0.1, L_y = 0.1$ and the thickness of the heat generation zone (Δx_{flame}) was set to 0.01 m . Table 3 shows the values of non-dimensional parameters used for this test case.

The values of gas temperature along the mid-plane section ($\eta_y = 0.5$) of the burner are shown in Figure 7. It is seen that the incoming air-fuel mixture is preheated by radiation in the upstream region of the combustion zone. The maximum temperature occurs inside the heat generation domain after which the gas temperature decreases by converting gas enthalpy into thermal radiation. As Figure 7 shows, there is a good agreement between the present results and those obtained theoretically in Ref. [27], even though different radiation models are used for radiation computations.

5. RESULTS AND DISCUSSION

Based on the principal of energy conversion between gas enthalpy and thermal radiation, a new type of three-layered porous heat exchanger was analyzed here. A schematical illustration of this PHE has been shown in Figure 1. Two Quartz glass windows are used to separate the porous layers from each other. Since the temperature of porous layers is not too high, a great part of emitted energy from porous media lies in the range of long wavelength (infrared). It should be noted that the wavelength range in thermal radiation is from about 0.1 to $100 \mu\text{m}$, therefore a special glass type as Hoya R-72 IR filter, which passes completely the wavelength of 720 nm and above is a suitable choice for this application [9]. Regarding the high transparency of this glass type for thermal radiation, it is assumed in the computations that the whole incident radiation towards the glass walls is completely transmitted without any reflection, absorption or emission.

The values of non-dimensional parameters of the present study have been given in Table 4. In three sections of the 2-D rectangular PHE under consideration, boundaries at locations $\eta_y = 0$ and $\eta_y = 1$ are kept insulated. Working gas temperature at the inlet section of the HT layer is 1000 K except for the case in which the effect of HT gas flow temperature on the performance of the PHE is studied. In addition, the value of aspect ratio $r = L_x / L_y$ is always kept at 1. In the analysis of the present PHE, there are many independent

TABLE 3. Non-Dimensional Parameters of the Test Case from Talukdar, et al [27].

Parameter	Value
P_1	102.80
P_2	666.45
P_3	3.33×10
P_4	0.00
P_5	0.00
P_6	103.48
Pe	38.91
Nu	400.00
Bi	5.00
B'_1	1.00
B'_2	1.00
α	0.00

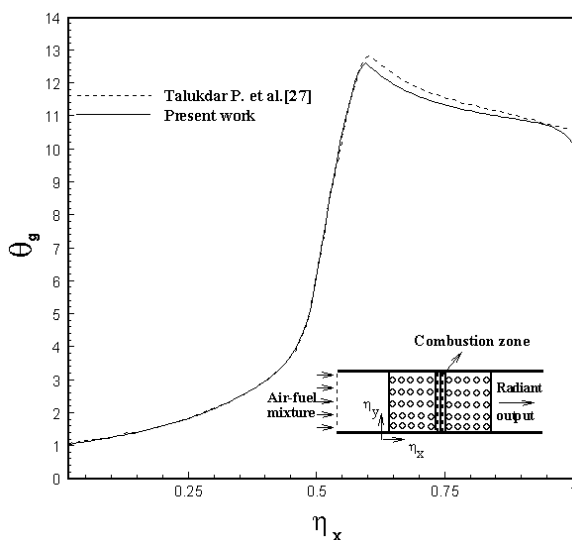


Figure 7. Gas temperature distribution along the porous radiant burner with uniform heat generation.

TABLE 4. Non-Dimensional Parameters of the Present Heat Recovery System [27].

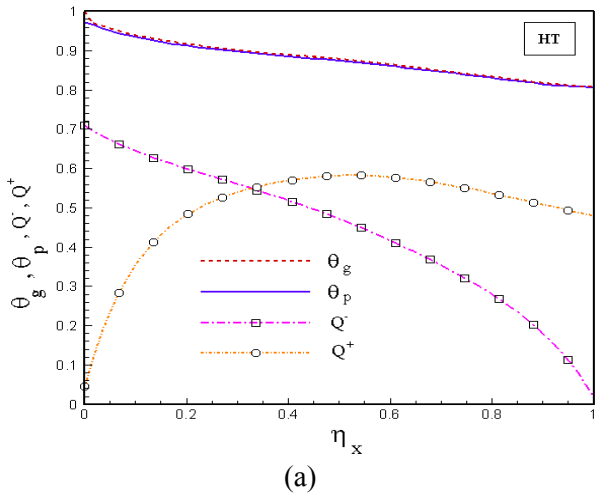
Parameter	Value
P_1	2.73×10^6
P_2	5.88
P_3	10.23×10^6
P_4	0.00
P_5	0.00
Pe	88.34
Nu	2074.69
Bi	15.00
B'_1	0.00
B'_2	0.00

parameters, but it is possible to present only some results for a wide range of conditions.

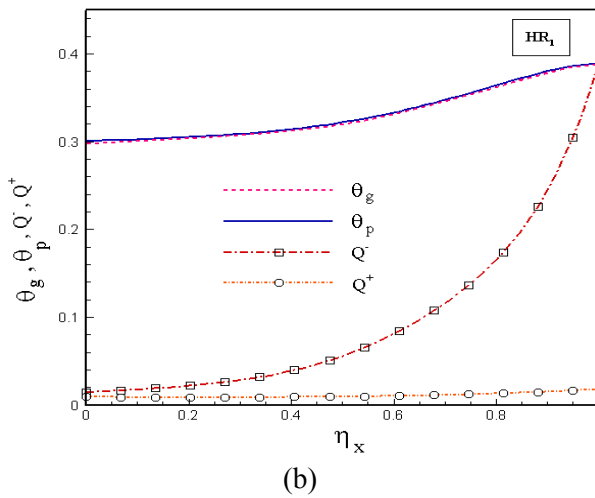
The gas and solid temperature distributions, θ_g and θ_p , and also the variation of radiative fluxes \bar{Q} and \bar{Q}^+ along the mid-plane ($\eta_y = 0.5$) of three sections of the PHE with $\tau_0 = 1$ have been shown in Figure 8. It can be seen that in the HT section, the gas enthalpy is converted into thermal radiation because of the sharp temperature decrease in the gas flow, and the recaptured radiations $\bar{Q}_{rad}(\eta_x = 0)$ and $\bar{Q}_{rad}(\eta_x = 1)$ are emitted into the porous layers in the HR₁ and HR₂ sections. As Figures 8b, 8c show, the porous medium in these sections is heated by absorbing the incoming radiations and the low temperature airflow is effectively heated by the reverse conversion from thermal radiation to gas enthalpy in two steps by passing through HR₁ and HR₂ sections, respectively. It is seen that in all three sections, the gas and porous temperature are very close to each other owing to the large convection coefficient such that the gas temperature is greater than the temperature of porous media in HT section and the reverse state is seen in HR₁ and HR₂ sections.

Gas temperature contours of the HR₂ section of the PHE have been shown in Figure 9. It is seen that, there is not any considerable variation in gas temperature along the y-axis. Furthermore, the non-regular curvature of the isotherms is because of the random variation of gas velocity according to the random location of square cylinders in different locations. In addition, the gas temperature rise along the flow direction can easily be seen through the porous segment.

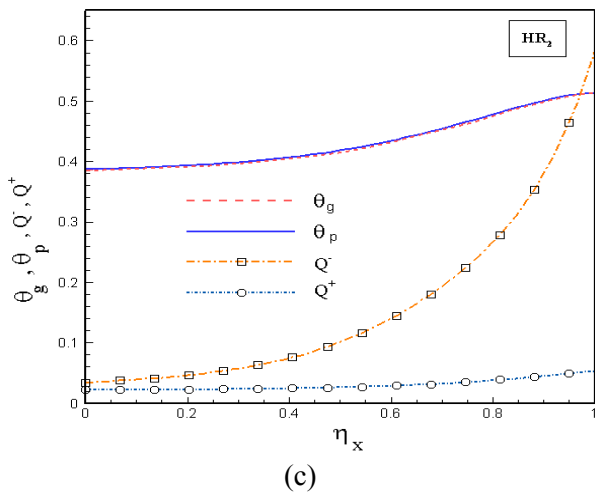
Figure 10 shows schematically an example of the inlet and outlet gas temperature in each section of the PHE under consideration for 1000 K level of T_{g_0} . Here, in this figure, each section corresponds to the space between vertical lines, which symbolically represent the separating and insulating walls. The arrows represent the flow directions of the HT, HR₁ and HR₂ sections. This figure also shows that the flow direction in the HT and HR₂ sections is the same and opposite to the flow direction in HR₁ section. Besides, it can be inferred from Figure 10 that the higher optical thickness results in more decrease in the temperature of



(a)



(b)



(c)

Figure 8. Distribution of gas and porous media temperature and radiative heat flux along the mid-plane of three layers of the PHE.

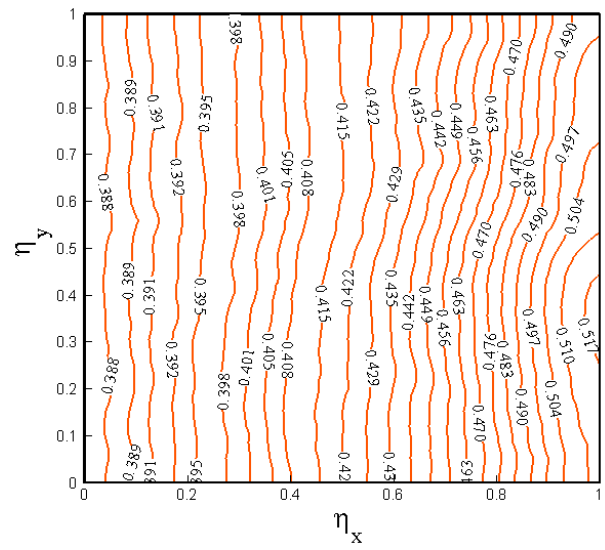


Figure 9. Gas temperature contours of the HR₂ section $\omega = 0, \tau_0 = 3$

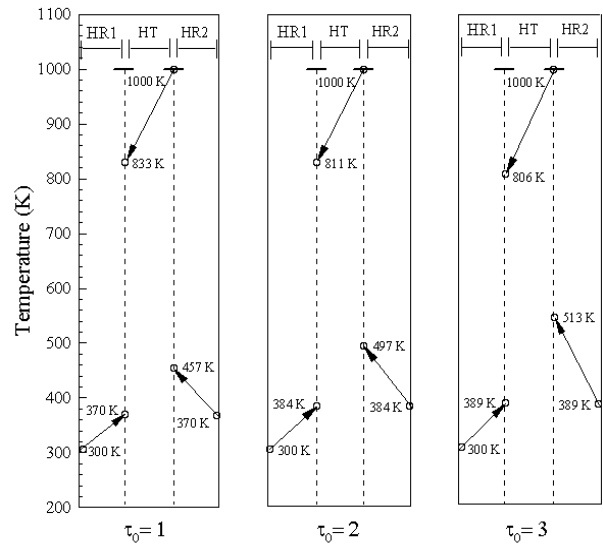


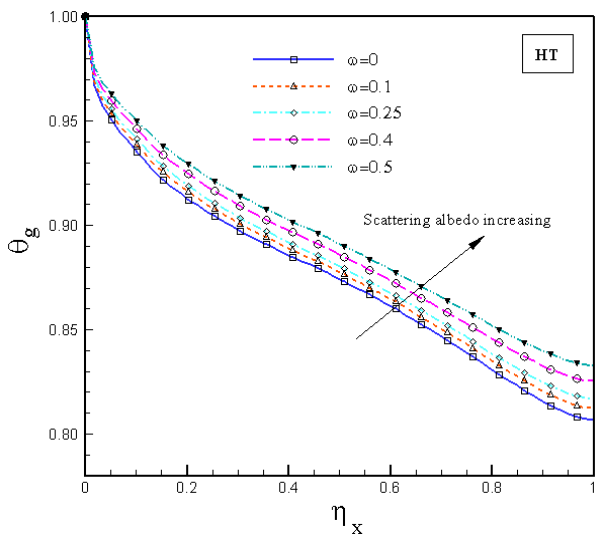
Figure 10. Schematic representation of the effect of o thickness on the gas temperature distribution in each section.

working gas of HT section and also more increase in the ones of HR₁ and HR₂ sections.

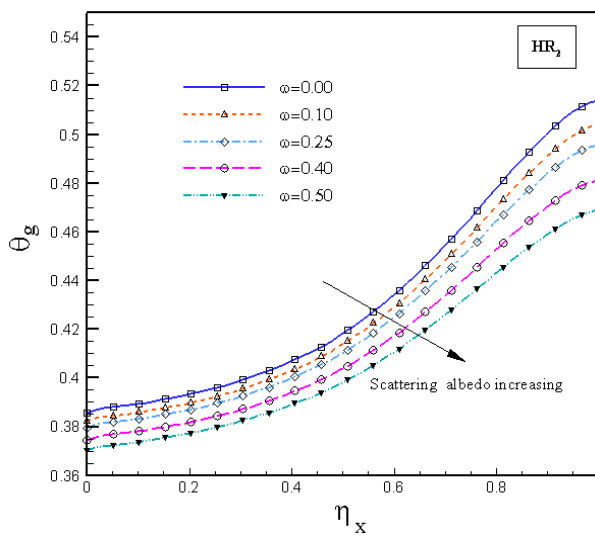
In order to show the effect of scattering albedo on the gas temperature distribution of HT and recovery sections, variation of gas temperature along the mid-plane ($\eta_y = 0.5$) of HT and HR₂ sections with scattering albedo has been shown in Figure 11. Figure 11a shows that increasing of

scattering albedo led to less temperature drop of working gas along the HT section which causes less energy conversion from gas enthalpy to thermal radiation. It can also be seen from Figure 11b that scattering albedo results in less temperature rise in the HR₂ section.

In the present study, the efficiency of PHE is



(a)



(b)

Figure 11. The effect of scattering albedo on the: (a) Gas temperature drop of the HT layer at mid-plane section and (b) Air temperature rise of the HR₂ layer at mid-plane section.

also computed to obtain the thermal performance of this system. Figures 12 and 13 show the effect of τ_0 , ω and inlet gas temperature to the HT section, T_{g_0} , on the PHE efficiency which is generally defined by the following equation:

$$\eta = \frac{\sum_{HR_1, HR_2} m_a c_a \Delta T_a}{m_g c_g (T_{g_0} - T_\infty)} \quad (51)$$

Where m_a , m_g , c_a and c_g are the mass flow rate and the specific heat at constant pressure of the air and gas flows, respectively. Also, ΔT_a is the air temperature increase along HR₁ and HR₂ sections and T_∞ is the ambient temperature which is equal to 300 K. Because in the computations, the physical properties of gas and air are considered equal to each other, with the same velocity along porous layers, the non-dimensional form of Equation 51 can be summarized as follows:

$$\eta = \frac{HR_1, HR_2 \Delta \theta_a}{(1 - \theta_\infty)} \quad (52)$$

It can be seen from Figure 12 that the PHE efficiency decreases with increasing scattering albedo. This figure also shows that the PHE efficiency increases with increasing the optical thickness of porous layers such that the optical thickness of about 4 seems to be enough to obtain the sufficient efficiency. In addition, the effect of T_{g_0} on the efficiency of PHE has been shown in Figure 13. Comparison between efficiency curves shows that the PHE efficiency increases when the temperature of inlet gas flow into the HT section becomes very high, especially for large optical thicknesses. It should be noted that as it is seen in Figure 13, this type of heat exchanger has very high efficiency which is well above that of conventional heat exchangers which is about 25 %.

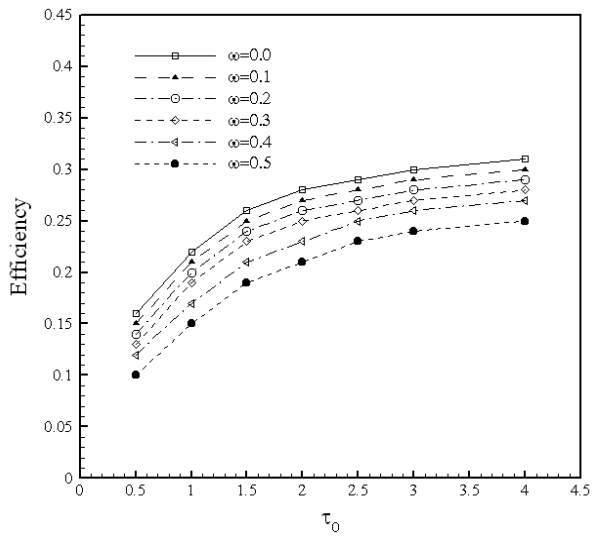


Figure 12. The effect of τ_0, ω on the PHE efficiency

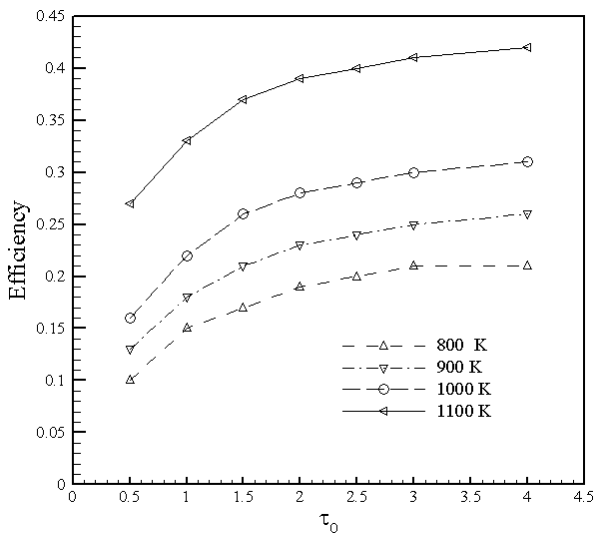


Figure 13. The effect of τ_0, T_{g_0} on the PHE efficiency $\omega = 0$.

6. CONCLUSIONS

Fluid flow simulation and thermal analysis of a 2-D porous heat exchanger was performed in the present study. This system, which works based on energy conversion between gas enthalpy and thermal radiation, has three distinct layers that are separated from each other by two quartz glass

walls. The energy conversion from gas enthalpy to thermal radiation takes place in HT section and the reverse conversion process occurs in recovery sections. The lattice Boltzmann method was used to simulate fluid flow through porous layers. Besides, heat transfer characteristics of the proposed PHE were investigated by solving the governing equations with the discrete ordinates method to determine the radiative heat flux distribution along porous layers. Furthermore, the effect of optical thickness and scattering albedo on the gas temperature distribution of HT and recovery sections and the efficiency of PHE was studied. It was found that this type of PHE has higher efficiency when porous layers with higher optical thickness and lower scattering albedo are used in the structure of the PHE. Finally, the effect of inlet gas temperature into HT section on the PHE efficiency was studied. Overall, the results show that this type of heat exchanger is efficient, although it has a very simple structure.

7. NOMENCLATURE

\cdot	surface area per unit volume (m^2/m^3)
$B_{1,2}$	incoming radiations (W/m^2)
$B'_{1,2}$	non-dimensional incoming radiations, $B_{1,2}/\sigma T_{g_0}^4$
Bi	Biot number, hL_x/k_p
c_s	sound speed
c_g	specific heat of gas ($J/kg^\circ C$)
d_p	obstacle size (m)
e	total energy
e_α	discrete particle velocity in LBM
f	density distribution function
F	fraction function
h	convective heat transfer coefficient ($W/m^2^\circ C$)
\cdot	intensity (W/m^2)
\cdot^*	non-dimensional intensity, $I/\sigma T_{g_0}^4$
\cdot	index of grids in y-direction
j_{max}	number of grids in y-direction

\dot{j}_x	flow momentum in x direction
\dot{j}_y	flow momentum in y direction
K_g	gas thermal conductivity ($W/m^\circ C$)
K_p	solid thermal conductivity ($W/m^\circ C$)
L_x	length of the porous medium (m)
L_y	height of the porous medium (m)
m	moment
Nu	Nussult number, hL_x/k_g
P	non-dimensional pressure, $\tilde{P}/\rho u_{g_0}^2$
\tilde{P}	pressure (pa)
p_{xx}	diagonal component of the stress tensor
p_{xy}	off-diagonal component of the stress tensor
P_1	dimensionless group, $hL_x A / \rho_g c_g u_{g_0} (\Delta x \Delta y)$
P_2	dimensionless group, $\frac{K_p/L_x}{\sigma T_{g_0}^3}$
P_3	dimensionless group, $hL_x A / \sigma T_{g_0}^3 (\Delta x \Delta y)$
P_4	dimensionless group, $h_{w_p} L_x / k_p$
P_5	dimensionless group, $h_{w_g} L_x / k_g$
Pe	Peclet number, $\rho_g u_{g_0} c_g L_x / k_g$
q_{rad}	radiative heat flux (W/m^2)
q_x	heat flux in x direction
q_y	heat flux in y direction
Q_{rad}	dimensionless radiative heat flux, $q_{rad} / \sigma T_{g_0}^4$
r	aspect ratio, L_x / L_y
Re_{L_x}	Reynolds number, $u_{g_0} L_x / \nu$
Re_{d_p}	Reynolds number, $u_{g_0} d_p / \nu$
\hat{s}_i	direction vector in RTE
T	temperature ($^\circ C$)
T_∞	ambient temperature ($^\circ C$)
T_{g_0}	gas temperature at duct's inlet ($^\circ C$)
u_g	velocity along x direction (m/s)
u_{g_0}	gas velocity at duct's inlet (m/s)

v_g	velocity along y direction (m/s)
\bar{U}	non-dimensional x velocity, u/u_{g_0}
\bar{V}	non-dimensional y velocity, v/u_{g_0}
x	coordinate along the flow direction (m)
X	non-dimensional length, L_x/L_y
y	coordinate perpendicular to the flow direction (m)

Greek Symbols

α	particle velocity direction
β	extinction coefficient, $\sigma_a + \sigma_s$
*	non-dimensional gradient operator, $L_x \nabla$
∇	$L_x \nabla$
Δx	grid spacing along x-axis (m)
Δy	grid spacing along y-axis (m)
Δ_{η_x}	non-dimensional grid spacing along x-axis, $\Delta x/L_x$
Δ_{η_y}	non-dimensional grid spacing along y-axis, $\Delta y/L_x$
δt	time step
δx	lattice spacing
\mathcal{E}	energy square
ε	emissivity
η_x	non-dimensional x coordinate, x/L_x
η_y	non-dimensional y coordinate, y/L_x
ν	kinematical viscosity (m^2/s)
ϕ	porosity
φ	scattering phase function
ρ_g	gas density (m^3/kg)
ρ_w	wall reflection coefficient
σ	Stephan-Boltzmann coefficient ($w/m^2 K^4$)
σ_a	absorption coefficient (m^{-1})
σ_s	scattering coefficient (m^{-1})
$\theta_{g,p}$	non-dimensional temperature, $T_{g,p}/T_{g_0}$
τ	non-dimensional relaxation time
τ_0	optical thickness, βL_x
τ_1	non-dimensional parameter, $\sigma_a L_x$

τ_2 non-dimensional parameter, $\sigma_s L_x$
 w weighting constant

Subscripts

b black body
 B bottom
 e exit of the porous matrix
 g gas
 i inlet of the porous matrix
 p solid
 T top

Superscripts

eq equilibrium
 in incoming velocity direction
 m outgoing radiation direction
 m' incoming radiation direction
 out outgoing velocity direction
 $+$ downstream direction
 $-$ upstream direction

Abbreviations

DOM discrete ordinates method
 HR heat recovery
 HT high temperature
 LBM lattice Boltzmann method
 PHE porous heat exchanger
 RTE radiative transfer equation

8. REFERENCES

- Echigo, R., "Effective energy conversion method between gas enthalpy and thermal radiation and application to industrial furnaces", *Proc. of the 7th Int. Heat Transfer Conference*, Munchen, Vol. 6, (1982), 361-366.
- Wang, K. Y. and Tien, C. L., "Thermal insulation in flow systems combined radiation and convection through a porous segment", *J. Heat Transfer*, Vol. 106, (1984), 453-459.
- Echigo, R., "Heat transfer augmentation in high temperature heat exchangers, in: High Temperature Equipment", Hemisphere, Washington, D.C., U.S.A., (1986), 41-72.
- Khoshtravan, E., "Heat transfer in a column of packed beds with spheres", *J. Engineering*, Vol. 2, No. 3,4, (1989), 152-159.
- Yoshida, H., Yung, J.H., Echigo, R. and Tomimura, T., "Transient characteristics of combined conduction, convection and radiation heat transfer in porous media", *Int. J. Heat and Mass Transfer*, Vol. 33, No. 5, (1990), 847-857.
- Gandjalikhan Nassab, S.A., "Transient characteristics of an energy recovery system using a porous medium", in: *Proc. Instn. Mech. Engrs., Part A., J. Power and Energy*, Vol. 216, (2002), 387-394.
- Tomimura, T., Hamano, T., Honda, Y. and Echigo, R., "Experimental study on a multi-layered type gas-to-gas heat exchanger using porous media", *Int. J. Heat and Mass transfer*, Vol. 47, (2004), 4615-4623.
- Gandjalikhan Nassab, S.A., "Thermal behavior of a new type of multi-layered porous air heater", *IJE Transactions A: Basics*, Vol. 19, No. 1, (2006), 87-94.
- Gandjalikhan Nassab, S.A. and Maramisaran, M., "Transient numerical analysis of a multi-layered porous heat exchanger including gas radiation effect", *Int. J. Thermal Sciences*, Vol. 48, (2009), 1586-1595.
- Keshtkar, M.M. and Gandjalikhan Nassab, S.A., "Theoretical analysis of porous radiant burners under 2-D radiation field using discrete ordinates method", *Journal of Quantitative Spectroscopy and Radiative Transfer*, Vol. 110, (2009), 1894-1907.
- Chen, S. and Doolen, G.D., "Lattice Boltzmann method for fluid flows", *Annu. Rev. Fluid Mech.*, Vol. 30, (1998), 329-64.
- Guo, Z. and Zhao, T. S., "Lattice Boltzmann model for incompressible flows through porous media", *Phys. Rev. E.*, Vol. 66, (2002), 036304_1 - 036304_9.
- S. Succi, E. Foti and F. Higuera. Three-dimensional flows in complex geometries with the lattice Boltzmann method, *Europhys. Lett.*, Vol. 10(5) (1989), 433 - 438.
- Cancelliere, A., Chang, C., Foti, E., Rothman, D.H. and Succi, S., "The permeability of a random medium: comparison of simulation with theory", *Phys. Fluids A.*, Vol. 2, No. 12, (1990), 2085-2088.
- Spaid, M.A.A. and Phelan, Jr. F. R., "Lattice Boltzmann methods for modeling micro-scale flow in fibrous porous media", *Phys. Fluids*, Vol. 9, (1997), 2468 - 73.
- Pan, C., Luo, L.-S. and Miller, C.T., "An evaluation of lattice Boltzmann schemes for porous medium flow simulation", *Computers and Fluids*, Vol. 35, No. 8/9, (2006), 898-909.
- Yan, W.W., Liu, Y., Xu, Y.S. and Yang, X.L., "Numerical simulation of air flow through a biofilter with heterogeneous porous media", *Bioresource Technology*, Vol. 99, (2008), 2156-2161.
- Nabovati, A., Llewellyn E.W. and Sousa A.C.M., "A general model for the permeability of fibrous porous media based on fluid flow simulations using the lattice Boltzmann method", *Composites A.*, Vol. (40), (2009), 860-869.
- Lallemand, P. and Luo, L.-S., "Theory of the lattice Boltzmann method: dispersion, dissipation, isotropy, *Galilean Invariance and Stability. Phys. Rev. E.*, Vol. 61, No. 6, (2000), 6546-6562.
- D'Humieres, D., Ginzburg, I., Krafczyk, M., Lallemand, P. and Luo, L.-S., "Multiple-relaxation-time lattice Boltzmann models in three dimensions", *Phil. Trans. R. Soc. Lond. A*, Vol. 360, (2002), 437-451.

21. Lim, C.Y., Shu, C., Niu, X.D. and Chew, Y.T., "Application of lattice Boltzmann to simulate micro channel flows", *Physics of Fluids*, Vol. 14, No. 7, (2002) 2299-2308.
22. Renken, K. and Poulidakos, D., "Experiment and analysis of forced convective heat transport in a packed bed of spheres", *Int. J. Heat and Mass Transfer*, Vol. 31, No. 7 (1988), 1399-1408.
23. Chou, F.C. and Lien, W. Y., "Forced convection in a parallel plate channel filled with packed spheres", *AIAA/ASME Thermo physics and Heat Transfer Conference*, HTD, Vol. 139, (1990), 57-64.
24. Rahimian, M.H. and Pourshaghagh, A., "Direct simulation of forced convection flow in a parallel plate channel filled with porous media", *Int. Comm. Heat Mass Transfer*, Vol. 29, No. 6, (2002), 867- 878.
25. Ben Kheder, C., Cherif, B. and Sifaoui, M.S., "Numerical study of transient heat transfer in semitransparent porous medium", *Renewable energy*, Vol. 27, (2002), 543-560.
26. Modest, M.F., "Radiative Heat Transfer, McGraw-Hill, New York, U.S.A., (2003).
27. Talukdar, P., Mishra, S.C., Trimis, D. and Durst, F., "Heat transfer characteristics of a porous radiant burner under the influence of a 2-D radiation field", *Journal of Quantitative Spectroscopy and Radiative Transfer*, Vol. 84, (2004), 527-537.